convenience, consider $TM_{0,p}$ modes with only an E_z component tangential to the wall. A nonzero value of E_z at the wall will drive a wall current according to Ohm's law:

$$j_z = \sigma E_z \tag{4.46}$$

Let us use this in Ampere's law (Equation 4.1), applied within the wall, assuming a wave with time dependence $e^{-i\omega t}$:

$$\left(\nabla \times B\right) \bullet \hat{z} = \mu_0 \sigma E_z - i\frac{\omega}{c^2} E_z \tag{4.47}$$

For walls of high conductivity, so that $\mu_0\sigma >> \omega/c^2 = \omega\mu_0\varepsilon_0$, we ignore the second term on the right side. Now, take the curl of Faraday's law (Equation 4.2) and use Equation 4.47 and the fact that there are no free charges, so that $\nabla \bullet \mathbf{E} = 0$:

$$\left[\nabla \times \left(\nabla \times E\right)\right] \bullet \hat{z} = -\nabla^2 E_z = i\omega\left(\nabla \times B\right) \bullet \hat{z} = i\omega\mu_0\sigma E_z \tag{4.48}$$

For convenience, model this as a one-dimensional planar situation, so that Equation 4.48 takes the form (with α to be determined shortly)

$$\frac{d^2 E_z}{dx^2} = -\alpha^2 E_z \tag{4.49}$$

with x measured from the wall, at x = 0, and increasing into the wall; this has the solution

$$E_z = E_0 e^{-\alpha x} \tag{4.50}$$

with E_0 the axial electric field at the wall, x = 0, and

$$\alpha = \frac{\left(1+i\right)}{2^{1/2}}\left(\omega\mu_0\sigma\right)^{1/2} \tag{4.51}$$

What we see is that the electric field drops off exponentially within the wall, and the phase is shifted as one moves into the wall. The distance scale for exponential field drop-off in the wall is known as the *skin depth*, δ, which is given by

$$\delta = \left(\frac{2}{\omega\mu_0\sigma}\right)^{1/2} = \frac{1}{\left(\pi\sigma\mu_0 f\right)^{1/2}} \tag{4.52}$$

As an example, in copper, $\sigma = 5.80 \times 10^7\ (\Omega\text{-m})^{-1}$ so that the skin depth at 1 GHz is 2.1 μm; scaling to other frequencies is as $f^{-1/2}$ (see Problem 6).

Next, consider the current per unit width flowing in the wall, which we define in our simplified one-dimensional model by

$$J_z = \int_0^\infty j_z dx = \int_0^\infty j_0 e^{-(1+i)x/\delta} dx = \frac{\delta}{1+i} j_0 \tag{4.53}$$

Now define a complex surface impedance of the conducting wall by

$$Z_s = \frac{E_0}{J_z} = \frac{E_0}{j_0}\left(\frac{1+i}{\delta}\right) = \frac{1}{\sigma\delta}\left(1+i\right) \tag{4.54}$$

The real part of this impedance is the *surface resistance*:

$$R_s = \frac{1}{\sigma\delta} = \left(\frac{\pi f \mu_0}{\sigma}\right)^{1/2} \tag{4.55}$$

Note that R_s has the dimensions of a resistance, although strictly speaking, it is not a resistance in the classical sense.

Next, consider the relationship between J_z and the tangential component of **B** at the wall. Starting with Ampere's law again, neglecting the so-called displacement current term, $(1/c^2)\,\partial\mathbf{E}/\partial t$, we integrate over the area perpendicular to the z axis that excludes the empty interior of the waveguide:

$$\iint \nabla \times B \bullet d = \oint B \bullet dl = \mu_0 \iint j \bullet dA \tag{4.56}$$

The transformation of the area integral to a closed line integral over the boundary of the area of integration is a direct consequence of Stokes' theorem. Assuming that the magnetic field drops to zero deep in the conductor and that symmetry causes the portions of the line integral perpendicular to the surface of the wall to vanish, the line integral becomes an integral over a path along the surface of the waveguide. Now for most cases of interest to us, the area integration on the far right-hand side of Equation 4.56 decomposes into separable integrations along the surface of the waveguide and

perpendicular to the surface of the waveguide, into the wall. This is clearly at least approximately the case for our rectangular and circular waveguides, where one can separate the dependences on x and y, or r and θ, into products of functions that depend only on x or y, or r or θ. Therefore, in a cylindrical waveguide, for example, for a TM mode, we can rewrite Equation 4.56 as

$$J_z = \frac{1}{\mu_0} B_\theta \tag{4.57}$$

where J_z is defined analogously to Equation 4.53 as the current per unit circumference at the waveguide wall.

Finally, we use the Poynting vector, $\mathbf{S} = \mathbf{E} \times \mathbf{H}$, to determine the power flow per unit length from the electromagnetic field into the wall per unit length, which is power lost to the resistivity of the wall. We denote this quantity W_L, and it is given by

$$W_{L,TM} = \frac{1}{2\mu_0} \mathrm{Re} \oint E_z(r_0) B_\theta(r_0) r_0 d\theta \tag{4.58}$$

where the integral is over the surface of the waveguide at $r = r_0$. Note that when the wall is perfectly conducting, $E_z(r_0) = 0$ and there is no power loss. As we found earlier, though, E_z no longer vanishes at the wall for finite σ, so that we can see how the power loss in the wall arises. Making use of Equations 4.54 and 4.57, remembering that we take the real part of the integral in Equation 4.58, we find

$$W_{L,TM} = \frac{1}{2} r_0 R_S \int_0^{2\pi} |J_z|^2 \, d\theta \tag{4.59}$$

which emphasizes the significance of the surface resistivity, R_s, in determining power losses to the wall. In finding J_z, we note that because σ is a large quantity, E_z in Equation 4.46 is a small quantity, of order σ^{-1}, while J_z and B_θ are of order unity, so that we find J_z from Equation 4.57. For TM modes in a circular waveguide, B_θ is given in Table 4.3. From the table and Equation 4.57, we find

$$|J_z|^2 = \frac{|D|^2}{Z_0^2} \left(\frac{f}{f_{co}}\right)^2 \left[J_p'(\mu_{pn})\right]^2 \sin^2(p\theta) \tag{4.60}$$

where, as usual, $Z_0 = 377\ \Omega$. Putting this expression into Equation 4.59 and using the identity $J_p'(\mu_{pn}) = J_{p-1}(\mu_{pn})$, we get

$$W_{L,TM} = \frac{\pi}{2Z_o^2} r_0 R_s \left(\frac{f}{f_{co}}\right)^2 |D|^2 \left[J_{p-1}(\mu_{pn})\right]^2 \tag{4.61}$$

At this point, we want to eliminate D in favor of the power carried by the waveguide. To do so, we return to Equation 4.39:

$$P_{TM} = \frac{1}{2\mu_0} \int_0^{r_0} r dr \int_0^{2\pi} d\theta \left(\mathbf{E} \times \mathbf{B}^*\right) \bullet \hat{z} = \frac{1}{2\mu_0} \int_0^{r_0} r dr \int_0^{2\pi} d\theta \left(E_r B_\theta^* - E_\theta B_r^*\right) \tag{4.62}$$

Using the expressions for the field quantities in Table 4.3, performing the integral in Equation 4.62, and solving for D, Equation 4.61 becomes

$$W_{L,TM} = \frac{2}{r_0} \left(\frac{R_s}{Z_0}\right) \frac{P_{TM}}{\left[1 - (f_{co}/f)^2\right]^{1/2}} \tag{4.63}$$

From this quantity, which is the loss per unit length along the axis, we can compute the average loss per unit area in the wall:

$$\frac{\langle P_{L,TM} \rangle}{A} = \frac{W_{L,TM}}{2\pi r_0} = \frac{1}{\pi r_0^2} \left(\frac{R_s}{Z_0}\right) \frac{P_{TM}}{\left[1 - (f_{co}/f)^2\right]^{1/2}} \tag{4.64}$$

Because of the power loss in the wall, the power carried along the waveguide will also decline exponentially with distance along the waveguide:

$$P_{TM}(z) = P_0 e^{-2\beta z} \tag{4.65}$$

In this expression,

$$\text{TM modes: } \beta_{TM} = \frac{W_{L,TM}}{2P_{TM}} = \frac{1}{r_0} \left(\frac{R_s}{Z_0}\right) \frac{1}{\left[1 - (f_{co}/f)^2\right]^{1/2}} \tag{4.66}$$

The derivation of the corresponding expressions for TE waves proceeds analogously, taking account of the fact that the wall current flows in response to both tangential magnetic field components, B_θ and B_z. In this case,

$$W_{L,TE} = \frac{2}{r_0}\left(\frac{R_s}{Z_0}\right)\left[\left(\frac{f_{co}}{f}\right)^2 + \frac{n^2}{\mu_{pn}^2 - n^2}\right]\frac{P_{TE}}{\left[1-\left(f_{co}/f\right)^2\right]^{1/2}} \tag{4.67}$$

$$\frac{\langle P_{L,TE}\rangle}{A} = \frac{W_{L,TE}}{2\pi r_0} = \frac{1}{\pi r_0^2}\left(\frac{R_s}{Z_0}\right)\left[\left(\frac{f_{co}}{f}\right)^2 + \frac{n^2}{\mu_{pn}^2 - n^2}\right]\frac{P_{TE}}{\left[1-\left(f_{co}/f\right)^2\right]^{1/2}} \tag{4.68}$$

$$\text{TE modes: } \beta_{TE} = \frac{1}{r_0}\left(\frac{R_s}{Z_0}\right)\left[\left(\frac{f_{co}}{f}\right)^2 + \frac{n^2}{\mu_{pn}^2 - n^2}\right]\frac{1}{\left[1-\left(f_{co}/f\right)^2\right]^{1/2}} \tag{4.69}$$

A plot of β for several modes in a copper waveguide is shown in Figure 4.8. Remember that β gives us the rate at which the *fields* decrease exponentially with distance along a waveguide with small, but nonzero, resistivity in the wall material, while the power drops exponentially at twice this rate, according to Equation 4.65. Note that the quantities we have derived involve dimensionless ratios except for the inverse dependence on the waveguide radius and area, so that the units in these expressions depend only on the units with which we measure the waveguide radius. We see that this quantity diverges near the cutoff frequency. In fact, physically, we expect that as the group velocity drops to zero at the cutoff frequency, the electromagnetic energy quits propagating along the line, so that the wave, in a sense, sits

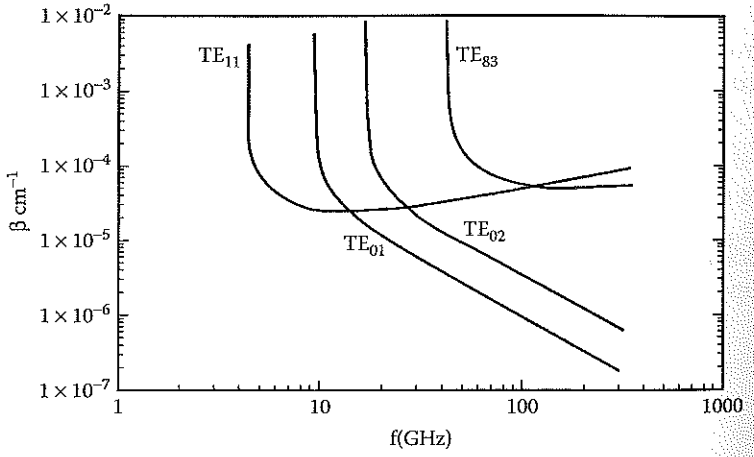

FIGURE 4.8
The attenuation coefficients for the fields and power in a waveguide with lossy walls having the conductivity of copper.

and dissipates its energy. We caution the reader, though, that our expression is not completely accurate in the vicinity of the cutoff frequency, since our underlying approximations begin to break down in this region.

Of course, all of the foregoing relationships between the power and the wall field strengths and between the power and the power dissipated in the walls are single-mode relationships linking the power and electric field for a given mode. As the cross section increases, multiple modes will become available to carry power in the waveguide, and the power density summed across all modes will become important. Regarding power density, a trade-off is many times involved: one would like to limit the number of modes available at the signal frequency in a waveguide or cavity, either to cut off propagation between cavities in a klystron or klystron-like device altogether or to inhibit competition between modes in the generation and transmission of power. As we have shown, in principle, any mode with a cutoff frequency below the frequency of an input signal can carry the wave energy; the exact apportionment of energy among the different modes is determined by the details of the coupling to the waveguide. Because ω_{co} decreases as the cross-sectional dimensions of a waveguide increase, a *single-mode waveguide* must be small enough to allow only one mode to be above cutoff for a given frequency. Achieving high power-handling capacity in HPM systems, however, frequently requires large cross-sectional areas, so that many modes lie above cutoff, particularly at the higher signal frequencies. Such waveguides are said to be *overmoded*, and special care must be taken to prevent energy transfer into unwanted modes. Many of the recent advances in HPM sources have focused on techniques for better control of parasitic modes in overmoded structures: waveguides, cavities, and beam–wave interaction regions.

4.4 Periodic Slow-Wave Structures

Let us return our attention to Figure 4.4 and recall a significant feature of the dispersion curves for both rectangular and circular waveguides: the phase velocity along the waveguide, ω/k_z, of all of the normal modes for rectangular and circular waveguides is greater than the speed of light, c. To be sure, the group velocity for each mode, $\partial\omega/\partial k_z$, lies between –c and c, so that no wave carries energy along the waveguide at a speed greater than the speed of light. Nevertheless, the superluminal phase velocities (i.e., greater than c) present a limitation because, as we shall see, they do not allow interactions with space-charge waves with phase velocities less than c.

The solution to this limitation is to introduce a periodic variation in some property of the waveguide in order to reduce the phase velocities below the speed of light, thus creating normal modes known as *slow waves*. This might involve periodically loading the waveguide with a resonant cavity, or winding a helically wound wire around the inner wall of the waveguide, or

periodically varying the radius of the waveguide. In fact, loading a waveguide with resonators spaced azimuthally around the wall is how the interaction region for magnetrons, including relativistic magnetrons, is constructed. The use of slow-wave structures (SWSs) constructed by wrapping a helical winding around the beam transport region, while common in conventional microwave devices operating at subrelativistic voltages (i.e., well below 500 kV), is not seen in relativistic microwave sources, presumably because of concerns about breakdown between turns in the winding at high power and large DC fields. In addition, the low phase velocities that can be achieved with a helix are simply not needed in relativistic devices, as we shall see. On the other hand, periodic variation of the wall radius in relativistic Cerenkov devices (Chapter 9), as well as in Bragg reflectors and mode converters, is a very common configuration.

4.4.1 Axially Varying Slow-Wave Structures

Let us consider this last method of producing a slow-wave structure first. We will only sketch out the process of deriving a dispersion relation, leaving the rather complicated derivation for such devices to the reader who wishes to consult the references.[2-6] The important point is that for slow-wave structures of this kind in relativistic electron beam devices, because the electron velocity is almost c, the waves need not be slowed to any great degree. Therefore, the variation in the wall radius is rather small, so that it can be treated as a small perturbation of a smooth-walled circular waveguide.

For simplicity, we consider variations of the wall radius with distance along the axis of period z_0, assuming no variations with θ,

$$r_w(z) = r_w(z + z_0) \tag{4.70}$$

although we note that structures can vary helically, also. As a consequence of Equation 4.70, the radian frequency of the normal electromagnetic modes of the slow-wave structure ω is a periodic function of the axial wavenumber k_z:

$$\omega(k_z) = \omega(k_z + mh_0) = \omega(k_m) \tag{4.71}$$

where m is any integer, $k_m = k_z + mh_0$, and

$$h_0 \equiv \frac{2\pi}{z_0} \tag{4.72}$$

Consider TM modes and further assume no azimuthal variation (i.e., p = 0); in this case, the only nonzero electromagnetic field components are the radial and axial electric field components, E_r and E_z, and the aximuthal magnetic field component B_θ. The periodicity of the system allows us to employ Floquet's theorem to write E_z as a sum of terms:

$$E_z = \sum_{m=-\infty}^{\infty} E_{zm}(r) e^{i(k_m z - \omega t)} = \left[\sum_{m=-\infty}^{\infty} E_{zm}(r) e^{imh_0 z} \right] e^{i(k_z z - \omega t)} \tag{4.73}$$

Note here that Floquet's theorem essentially amounts to expanding the field in a Fourier series, which is required to match the boundary conditions in Equations 4.5 and 4.6 at the periodically varying boundary of the slow-wave structure. Each of the other field components can be written in a sum of the same form; for each term of the sum at a given value of m, the components are related by relations of the form shown in Table 4.3, with k_z replaced by k_m, and $k_\perp$ replaced by $k_{\perp m}$:

$$k_{\perp m}^2 = \frac{\omega_{co,m}^2}{c^2} = \frac{\omega^2}{c^2} - k_m^2 \tag{4.74}$$

Therefore, as an example,

$$E_{rm} = i \frac{k_m}{k_{\perp m}^2} \frac{\partial E_{zm}}{\partial r} \tag{4.75}$$

In the sum for E_z, each function E_{zm} obeys a differential equation like Equation 4.34, so that, from Table 4.3,

$$E_{zm} = A_m J_0(k_{\perp m} r) \tag{4.76}$$

At this point, the derivation for TM waves in a periodic slow-wave structure diverges from that of the smooth-walled circular waveguide because, in general, $k_{\perp m} \neq \mu_{0n}/r_0$.* Rather, we need to find a different dispersion relation between ω and k_z. The process by which this is done is recounted in a number of the references. In short, we find the unit tangent and unit normal vectors for the surface of the slow-wave structure; the direction of these unit vectors $\mathbf{n}_t$ and $\mathbf{n}_p$ is straightforwardly determined from the shape of the wall, given by $r_w(z)$, so that $\mathbf{n}_t$ and $\mathbf{n}_p$ will depend on z. We then use these vectors in Equations 4.5 and 4.6, also using the solution for E_{zm} in Equation 4.76 and the expressions for the other field quantities derived from

* For clarity, we point out that m is an index on the so-called spatial harmonics in the periodicity relation of Equation 4.70 and the sum in Equation 4.72, while n is the index on the radial ordering of roots of the Bessel functions J_0. By assumption, the azimuthal index p has been chosen to be equal to 0.

E_{zm}, applying them at $r_w(z)$. To avoid having to deal with the z variation of the resulting expressions, we invert the Fourier transform that we employed in Equation 4.74, for example, multiplying the boundary condition for the tangential component of **E** by $\exp(-ilh_0)$ and integrating over z from $-z_0/2$ to $z_0/2$. When we do so, our boundary conditions can be written as a linear algebraic expression of the form

$$\mathbf{D} \bullet \mathbf{A} = 0 \tag{4.77}$$

where **D** is an infinite-dimensional matrix with elements give by

$$D_{lm} = \left(\frac{\omega^2 - k_l k_m c^2}{k_{\perp m}^2 c^2} \right) \int_{-z_0/2}^{z_0/2} e^{i(m-l)h_0 z} J_0\left[k_{\perp m} r_w(z) \right] dz \tag{4.78}$$

and **A** is an infinite-dimensional vector whose elements are the amplitude factors A_m in Equation 4.76. In order for a solution to exist for the vector **A** in Equation 4.77, it must be true that

$$\det [\mathbf{D}] = 0 \tag{4.79}$$

Note that the matrix elements depend on the shape of the wall perturbation through the term in the argument of the Bessel function in the integral. In Figure 4.9, we plot ω vs. k_z for the particular case of a sinusoidally rippled slow-wave structure, for which

$$r_w(z) = r_0 + r_1 \sin(h_0 z) \tag{4.80}$$

with $r_0 = 1.3$ cm, $r_1 = 0.1$ cm, and $z_0 = 1.1$ cm. In the plot, we have let k_z run over the interval from 0 to h_0; the plot is periodic in k_z if we extend the interval. Note that slow waves with $|\omega/k_z| < c$ have been created by the periodicity in Equation 4.71. As we shall discuss, the plot shown there is only approximately correct because of convergence issues with the use of the expansion in Equation 4.73.

The dispersion relation given by Equations 4.78 and 4.79 is clearly more complicated than that for TM waves in circular waveguides with constant radius; however, one can construct an approximate version of the plot shown in Figure 4.9 by properly connecting a set of dispersion diagrams for constant-radius waveguide modes, with wavenumbers properly shifted by multiples of h_0, as shown in Equation 4.71. An example application of this process for the lowest four modes of a sinusoidally rippled slow-wave structure is shown by the solid curves in Figure 4.10.[6] The broken curves in the figure are the dispersion curves of three spatial harmonics of the TM_{0m} modes of a smooth-walled waveguide with constant radius, $r_w = r_0$:

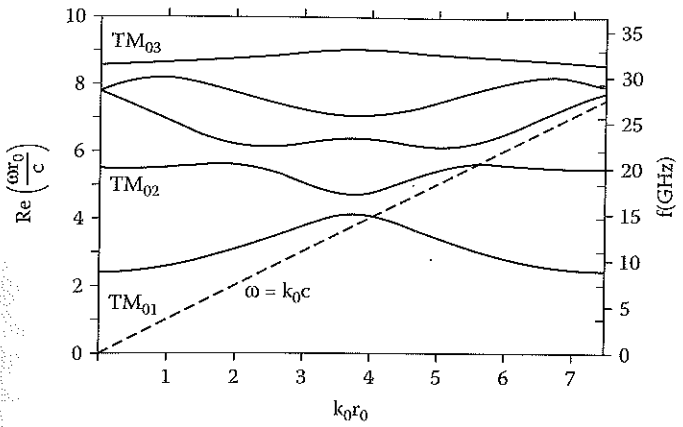

FIGURE 4.9
Dispersion relation computed from Equation 4.79, with $z_0 = 1.1$ cm, $r_0 = 1.3$ cm, and $r_1 = 0.1$ cm in Equation 4.80. (From Swegle, J.A. et al., *Phys. Fluids*, 28, 2882, 1985. With permission.)

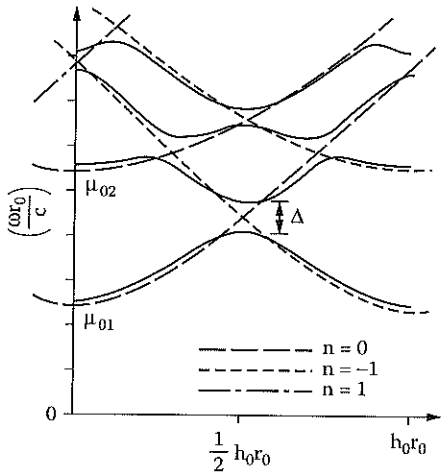

FIGURE 4.10
Construction of the slow-wave-structure dispersion curves from the shifted smooth-walled waveguide curves. These curves are periodic in k_z with period h_0. (From Leifeste, G.T. et al., *J. Appl. Phys.*, 59, 1366, 1986. With permission.)

$$\omega^2 = k_m^2 c^2 + \omega_{co}^2(0,n) \tag{4.81}$$

shifted for three values of m (= –1, 0, 1) in $k_m = k_z + mh_0$. In this expression, since we are considering smooth-walled waveguide modes, the cutoff frequencies are as given in Table 4.3:

$$\omega_{co}(0,n) = \frac{\mu_{on} c}{r_0}$$

When we examine the figure, intuition tells us — and analysis of the dispersion relations shows — that the periodic dispersion curves for the slow-wave structure can be approximated to generally acceptable accuracy by properly connecting the spatial harmonics of the smooth-walled waveguide in Equation 4. 81. Three simple rules govern this process:

1. Curves are constructed from the lowest frequency upward.
2. Every shifted smooth-wall curve is used, and each section of a smooth-wall curve is used only once.
3. SWS dispersion curves for different modes do not intersect. At intersections between the shifted smooth-wall curves, one jumps from one smooth-wall curve to another in tracing the structure curves, leaving a gap between the structure curves that increases in width with r_1/r_0, the relative depth of the wall perturbation.

Note that each curve for the SWS, unlike those for the smooth-wall modes, is limited to a finite range of frequencies, called a *passband*. Passbands for different modes may overlap in frequency. The spatial configurations of the electromagnetic fields associated with a mode will be similar to those of the nearest smooth-wall curve. Thus, a mode might have the characteristics of a TM_{01} mode for one range of k_z, and those of a TM_{02} mode over a different range of k_z (see Problem 7).

Except in the vicinity of the intersection of two smooth-walled curves of the form in Equation 4.81 for different values of axial index m or radial index n [through $\omega_{co}(0, n)$], the dispersion relation for a slow-wave structure is generally well approximated by the nearest smooth-walled waveguide curve of Equation 9.5. Further, the radial variation of the mode pattern for the slow-wave mode is quite similar to that for the closest smooth-walled waveguide mode. Because ω_{co} scales with $1/r_0$ and the periodicity of the dispersion curve scales as $h_0 = 2\pi/z_0$, to lowest order, the dispersion properties of the slow-wave structure are dominated by the average structure radius and its periodicity. The band gaps between modes where two smooth-wall modes intersect and the coupling of the beam and the structure, on the other hand, increases with the ratio r_1/r_0 for a structure such as that of Equation 4.80.

For sinusoidally rippled walls, it has been proven that the series in Equation 4.73, which is based on the so-called *Rayleigh hypothesis*, fails to converge when $h_0 r_1 = 2\pi(r_1/z_0) > 0.448$.[7,8] Comparing the results of calculations using Equation 4.73 with results obtained by numerically solving Maxwell's equations with no assumption of a Floquet expansion, Watanabe et al. found that the dispersion relation in Equation 4.79, with matrix elements given in Equation 4.78, is quite accurate at $h_0 r_1 \sim 5 \times 0.448$.[9] The solutions for the electromagnetic field quantities within the rippled-wall structure derived using a Floquet expansion, however, are noticeably different from the quantities determined by numerical solution of Maxwell's equations. Toward the center of the rippled-wall slow-wave structure, though, the fields computed by the two methods are more similar to one another, so that the effect of the fields on a beam would be approximately the same using either method.

4.4.2 Azimuthally Varying Slow-Wave Structures

In the axially varying slow-wave structures used in Cerenkov devices such as the relativistic backward wave oscillators (BWOs) of Chapter 8, the periodic variation in the wall radius is typically relatively small. In the azimuthally varying slow-wave structures found in magnetrons, on the other hand, the azimuthal variations are substantial. In fact, the slow-wave structure in a magnetron usually consists of N resonators spaced around a cylindrical, or as it is many times known, *reentrant* cavity. A simple example of such a cavity is shown in Figure 4.11. One can see that the volume of a resonator is comparable, although somewhat smaller, than the volume of the central coaxial cavity. Therefore, the technique for deriving a dispersion relation for a magnetron is qualitatively different than that used for an axially varying SWS in a BWO.

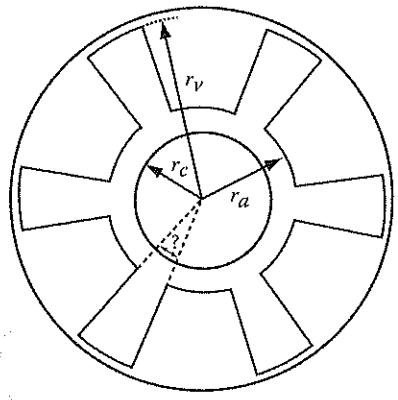

FIGURE 4.11
Cross section of a magnetron, with r_c the cathode radius and r_a the anode radius.

In a magnetron, for simplicity, we neglect axial field variations to lowest order, so that the fields vary only with radius and azimuthal angle, θ. The nonzero field components are E_r, E_θ, and B_z. The two key features of the analytical approach to deriving the dispersion relation for the azimuthally varying slow-wave structure in a magnetron[10] are the following: (1) the electromagnetic fields in the side resonators and in the central coaxial cavity are derived separately, usually under the assumption that the azimuthal electric field E_θ is a constant across the gap where the resonator opens into the central coaxial cavity at $r = r_a$; and (2) the dispersion relation itself results from the resonance that occurs when the admittances of the resonator Y_{res} and the central coaxial cavity $Y_{coaxial}$ add to zero at the gap where the resonator joins the central cavity at $r = r_a$:

$$Y_{res} + Y_{coaxial} = 0 \tag{4.82}$$

where the admittances at the gap are defined by

$$Y = \frac{h\int_{gap} E_\theta H_z d\ell}{\left|\int_{gap} E_\theta d\ell\right|^2} = \frac{h\int_{gap} E_\theta B_z d\theta}{\mu_0 r_a \left|\int_{gap} E_\theta d\theta\right|^2} \tag{4.83}$$

In this expression, the integral is across the gap at $r = r_a$, h is the length of the gap in the axial direction, and $H_z = B_z/\mu_0$. The numerator in the expression is the radial flow of power using the Poynting vector, and the denominator is analogous to a voltage across the gap; since power is proportional to the product of voltage and current, the admittance does indeed have units of resistance^{-1}. According to Kroll,[10] the gap admittance calculated using the fields in a side resonator is given by

$$Y_{res} = i\frac{h}{\psi r_a Z_0}\left[\frac{J_0(kr_a)N_1(kr_v) - J_1(kr_v)N_0(kr_a)}{J_1(kr_a)N_1(kr_v) - J_1(kr_v)N_1(kr_a)}\right] \tag{4.84}$$

where $Z_0 = 377\ \Omega$, ψ is the opening angle of the gap, as shown in Figure 4.11, $k = \omega/c$, and J and N are the Bessel functions of the first and second kind. Note here that Y_{res} is independent of θ, so that it is the same for each of the N resonators in the device. The admittance is a periodic function of k, although the Bessel functions somewhat obscure the real physics involved. The resonator is similar to a rectangular slot resonator with a constant spacing between conducting walls, d, shown in Figure 4.12. The admittance for this rectangular slot resonator is

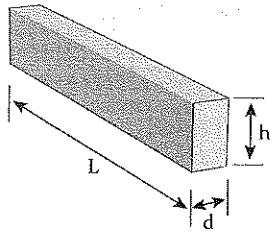

FIGURE 4.12
Dimensions of a rectangular slot resonator.

$$Y_{slot} = -i\frac{h}{dZ_0}\cot an(kL) \tag{4.85}$$

Here, we can clearly see the periodicity, as well as the fact that the admittance has zeroes wherever kL is an odd multiple of π/2 and poles (where $Y_{slot} \to \infty$) at multiples of π.

Calculating the admittance of the central coaxial cavity is a more complex process. We see that the coaxial cavity will have a periodic boundary condition on the azimuthal electric field at the anode radius $r = r_a$. We therefore construct our field solutions using a Fourier expansion in θ, writing them in the form, for example,

$$E_\theta(r,\theta,t) = \left[\sum_{s=-\infty}^{\infty} E_{\theta s}(r)e^{is\theta}\right]e^{i(p\theta-\omega t)} \tag{4.86}$$

Note here that s is the index on the Fourier expansion, analogous to the index m in Equation 4.74 for axially periodic systems, while p is the azimuthal mode number of the solution, analogous to k_0 in Equation 4.74. Solving Maxwell's equations in the coaxial region, with $E_\theta = 0$ at $r = r_c$, yields solutions of the form

$$E_{\theta s}(r) = A_s\left[J_s'(kr) - \frac{J_s'(kr_c)}{N_s'(kr_c)}N_s'(kr)\right] \tag{4.87}$$

In this expression $J_s' = dJ_s(x)/dx$, and similarly for N_s'. The expression in Equation 4.87 gives one term in the expansion of Equation 4.86. The expressions for E_r and B_z are derived from E_θ in a straightforward fashion. To write an expression for the boundary condition on E_θ at $r = r_a$, let us introduce one more index in order to number the N side resonators from q = 0 to q = N − 1. Now, E_θ vanishes at the conducting wall at $r = r_a$, except in the gaps of

the resonators, where it has the fixed magnitude E, but is phase shifted from gap to gap:

$$E_\theta\left(r=r_a,\theta\right)=Ee^{i(2\pi p/N)q},\ \frac{2\pi q}{N}-\frac{\psi}{2}\le\theta<\frac{2\pi q}{N}+\frac{\psi}{2} \tag{4.88}$$

It is a straightforward process to compute the constants in the Fourier expansion of Equation 4.86, A_s from Equation 4.87, using the boundary condition at $r = r_a$ and inverting the Fourier transform. The result from Kroll[10] is

$$E_\theta\left(r,\theta\right)=\frac{EN\psi}{\pi}\sum_{m=-\infty}^{\infty}\frac{\sin\left(s\psi\right)}{s\psi}\left[\frac{J_s'\left(kr\right)N_s'\left(kr_c\right)-J_s'\left(kr_c\right)N_s'\left(kr\right)}{J_s'\left(kr_a\right)N_s'\left(kr_c\right)-J_s'\left(kr_c\right)N_s'\left(kr_a\right)}\right]e^{is\theta}, \tag{4.89}$$

$$s=p+mN$$

Note here that we have suppressed the time dependence for convenience, and only specific values of the index s are allowed, a consequence of the symmetry of the azimuthal boundary condition. Computing H_z from this value of E_θ, one then computes the gap admittance using the coaxial cavity fields, which is shown in the reference to be

$$Y_{coaxial}=i\frac{Nh}{2\pi r_aZ_0}\sum_{m=-\infty}^{\infty}\left[\frac{\sin\left(s\psi\right)}{s\psi}\right]^2\left[\frac{J_s\left(kr_a\right)N_s'\left(kr_c\right)-J_s'\left(kr_c\right)N_s\left(kr_a\right)}{J_s'\left(kr_a\right)N_s'\left(kr_c\right)-J_s'\left(kr_c\right)N_s'\left(kr_a\right)}\right] \tag{4.90}$$

In addition to the geometric parameters N, h, ψ, r_c, and r_a, this expression depends on the frequency, through $k = \omega/c$ and the mode number p. One can easily show that in Equation 4.90, the admittance for a given value of p is the same as that for N – p.

To find the normal-mode frequencies for a given mode number p, one sets $Y_{coaxial}$ in Equation 4.90 equal to $-Y_{res}$ in Equation 4.84. This equation must be solved numerically, but we can visualize the solutions graphically if we plot the admittances as a function of k. First, Figure 4.13 is a qualitative depiction of the dependence of $Y_{coaxial}$ alone as a function of the normalized variable kr_a for an eight-resonator system (i.e., N = 8). Because $Y_{coaxial}(p) = Y_{coaxial}(N - p)$, only the values for p equal to 0 through 4 are shown. Analysis of Equation 4.90 shows that there are an infinite number of poles and zeroes for the admittance; in the figure, only the poles at k = 0 for p = 0 and at $k \cong 2/(r_a + r_c)$ for p = 1 are shown. Note that this latter pole occurs when $k \sim 2\pi/\lambda \cong 2/(r_a + r_c)$, where λ is the wavelength in the azimuthal direction. Thus, this pole occurs when λ is approximately equal to the circumference of the central coaxial cavity.

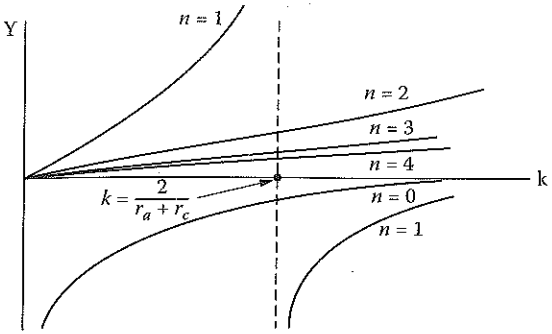

FIGURE 4.13
Qualitative depiction of the dependence of $Y_{coaxial}$ on k = ω/c. (From Kroll, N., *Microwave Magnetrons*, Collins, G.B., Ed., McGraw-Hill, New York, 1948. With permission.)

Figure 4.14 shows simultaneous plots of $Y_{coaxial}$ and $-Y_{res}$. The normal-mode values of k = ω/c are given by the intersections of the curves for each. The intersections labeled 1 through 4 are the lowest-order modes for the corresponding values of the azimuthal index p. The normal-mode frequency for p = 0 is ω = 0. The fact that there is no cutoff frequency above zero is a consequence of the coaxial geometry, in which there is no nonzero cutoff frequency (viewed another way, the modes are like transverse electromagnetic [TEM] modes of a coaxial waveguide that propagate all the way down to ω = 0). We can see that the normal-mode frequencies for the lowest-order modes climb toward a maximum value for p = N/2. This frequency must occur at a value of k less than the zero crossing for the curve of $-Y_{res}$. If we approximate Y_{res} by the rectangular slot expression in Equation 4.85, then the frequency for the p = N/2 mode must lie below $\omega_{max} \cong \pi c/2L$. The modes labeled 0_1 through 4_1 are the next-higher-order modes, and so on for 0_2 and

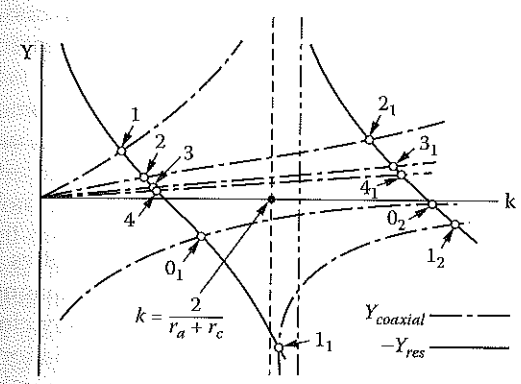

FIGURE 4.14
Qualitative depiction of the dependence of $Y_{coaxial}$ and $-Y_{res}$. The intersections between the two curves give the frequencies of the normal modes for the device. (From Kroll, N., *Microwave Magnetrons*, Collins, G.B., Ed., McGraw-Hill, New York, 1948. With permission.)

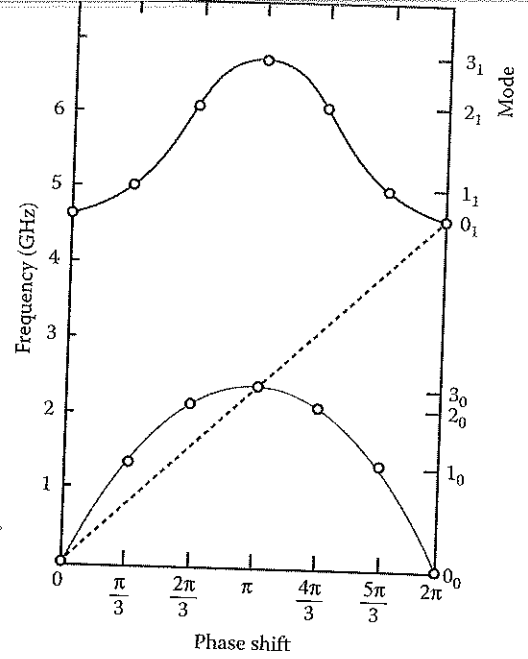

FIGURE 4.15
Dispersion relation for the A6 magnetron, with the phase shift on the horizontal axis $\Delta\phi = 2\pi(p/N)$. (From Palevsky, A. and Bekefi, G., *Phys. Fluids*, 22, 986, 1979. With permission.)

higher. The dispersion relation for the A6 magnetron with N = 6 and r_c, r_a, and r_v given by 1.58, 2.11, and 4.11 cm, respectively, is shown in Figure 4.15. Since $L = r_v - r_a = 2$ cm, $f_{max} = \omega_{max}/2\pi = 3.75$ GHz. By comparison, the $p = N/2 = 3$ mode (the so-called π-*mode*) frequency is $f_\pi = 2.34$ GHz, which is considerably lower than f_π. In Chapter 6, we will discuss the dispersion properties and their effect on device performance in greater detail.

4.5 Cavities

An important distinction between waveguides and cavities is that the latter are closed to some degree at the ends, so that electromagnetic radiation is trapped within them. Of course, they are not completely closed, or no radiation would escape, and the ratio of the amount of radiation trapped inside to the amount that escapes is one of the important properties of cavities.

One way to form a simple cavity is to take a section of waveguide and cap both ends with a conducting plate in order to trap the waves inside. Other examples of cavities are shown in Figure 4.16. If the walls and the endplates placed at z = 0 and z = L are perfectly conducting, the field

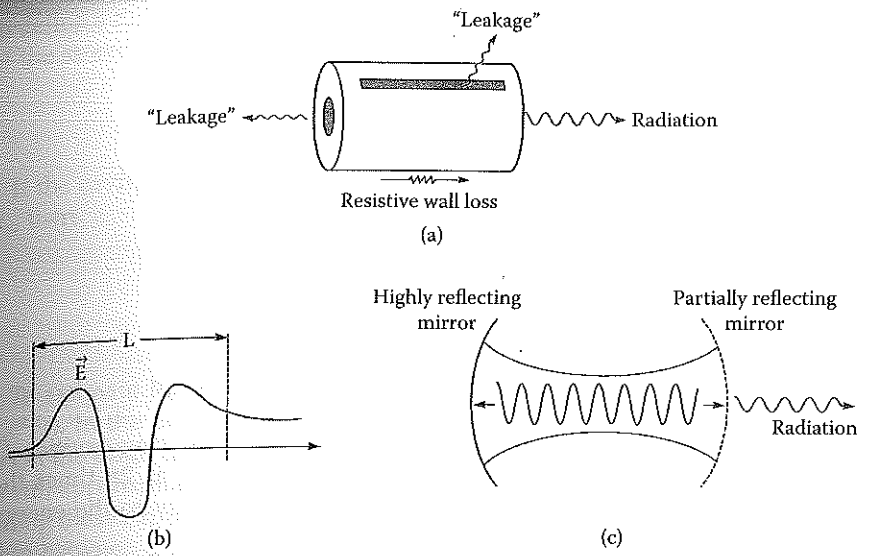

FIGURE 4.16
(a) Cylindrical cavity with partially open ends. Radiation from the right end is usefully extracted, while leakage and absorption in the wall resistance are loss channels. (b) An example of an electric field envelope in the cavity of (a); note the large field amplitude in the extraction region. (c) Quasi-optical cavity, with extraction through a partially reflecting mirror on the right.

components for a TM_{0n} wave, for example — E_r, E_θ, and B_z — must vanish at the ends, so that the electromagnetic waves in the cavity will be reflected there. Consequently, the axial wavenumber k_z, which was a free parameter in the infinitely long waveguide, will be restricted to certain discrete values in the cavity. In the expressions for E_r, E_θ, and B_z, we would replace $\exp(ik_z z)$ by $\sin(k_z z)$ and require $k_z L = q\pi$, with q any integer. This adds a third index to our designation of the cavity modes; for example, TM_{npq}. The dispersion curve for ω vs. k_z given in Figure 4.4 is now replaced by a set of points lying along the former curve, spaced $\Delta k_z = \pi/L$ apart. In actual practice, though, this ideal, if somewhat artificial, situation is modified, because of losses of energy from the cavity, either as intended radiation or as parasitic losses to nonzero wall resistance or to leakage through openings intended* or unintended. Therefore, if we speak of a resonance line for an ideal lossless, closed cavity with well-defined discrete values of k_z, then an open, lossy cavity has a nonzero spread in k_z (and, through the dispersion relation, ω) to its line width. If, for example, a small antenna were inserted into the cavity, the power coupled into and stored there would have a qualitative dependence on frequency like that shown in Figure 4.17.

*If two different modes are competing within a cavity, one might be suppressed by cutting slots in the wall at the location of minima in the fields of the desired mode so that the undesired mode "leaks out" of the cavity, or the slots might be oriented to suppress the flow of the RF wall currents supporting undesired modal field patterns.

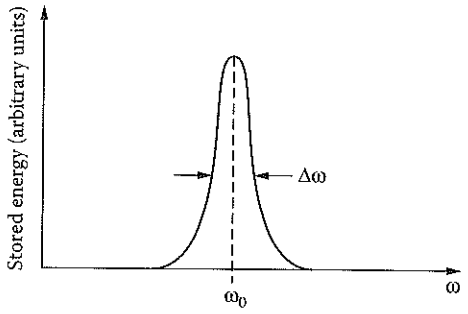

FIGURE 4.17
Stored energy in a cavity with nonzero line width about the line center ω_0.

These notions lead us to the *quality factor*, Q, characterizing cavities. Q is defined very generally, regardless of the cavity shape, as 2π times the ratio of the time-averaged field energy stored in the cavity to the energy lost per cycle:

$$Q = 2\pi \frac{\text{average stored energy}}{\text{energy lost per cycle}} = \omega_0 \frac{\text{average stored energy}}{\text{power loss rate}} \tag{4.91}$$

where ω_0 is the center frequency of the resonant line width of the cavity. This definition holds regardless of the cavity shape. In addition, one can show that Q is related to the resonance line width $\Delta\omega$ of Figure 4.17 by

$$Q = \frac{\omega_0}{2\Delta\omega} \tag{4.92}$$

We have described the power loss from a cavity as arising from two factors: radiated output power and parasitic losses.* Because power losses are additive, we can use the definition in Equation 4.92 to write

$$\frac{1}{Q} = \frac{1}{Q_r} + \frac{1}{Q_p} \tag{4.93}$$

with Q_r and Q_p representing the radiation and parasitic terms, respectively. Both factors will depend, of course, on the cavity configuration and the mode involved. To estimate the radiated contribution, Q_r, return to Equation 4.91 to define a radiated energy loss time constant from the cavity, T_r, as the ratio of the stored energy to the power lost from the cavity, in terms of which

$$Q_r = \omega_0 T_r \tag{4.94}$$

If the cavity has highly reflecting ends with reflection coefficients R_1 and R_2, then

$$T_r \approx \frac{L}{v_g\left(1 - R_1 R_2\right)} \tag{4.95}$$

To estimate the group velocity v_g, we write $\omega = \sqrt{\omega_{co}^2 + k_z^2 c^2}$, so that $v_g = k_z c^2/\omega$. In the limit of large values of k_z, that is, at short wavelengths, $v_g \approx c$. On the other hand, for small k_z or long wavelengths, where v_g is small, k_z is still approximately given by $q\pi/L$, with q the axial mode index. Incorporating these expressions into Equations 4.94 and 4.95, and using the relationship between ω and the free-space wavelength of the radiated microwaves λ, $\omega = 2\pi f = 2\pi/\lambda$, we estimate

$$Q_r \approx 2\pi \frac{L}{\lambda}\frac{1}{\left(1 - R_1 R_2\right)} \quad \text{(short wavelengths)} \tag{4.96a}$$

$$\approx 4\pi \frac{L^2}{\lambda^2}\frac{1}{q\left(1 - R_1 R_2\right)} \quad \text{(long wavelengths)} \tag{4.96b}$$

As an example, in a low-group-velocity device operated at long wavelengths near cutoff, such as a gyrotron, the long-wavelength limit applies. Such devices are sometimes referred to generally as diffraction generators, since output from the end is largely due to diffraction of the radiation from the (partially) open end. Providing Equation 4.96b holds for such diffraction generators with poorly reflecting end surfaces, the minimum radiative (diffraction-limited) Q of these devices for the lowest axial mode with q = 1 is $Q_{r,\min} = 4\pi L^2/\lambda^2$. We can see that Q_r decreases with the axial mode number; in other words, radiative losses from a cavity increase with the axial mode number. Overall, the radiative component of Q scales as a power of the length of the cavity measured in free-space wavelengths of the radiation.

Making a general estimate of the parasitic losses in a cavity is a difficult task, particularly when slotted or absorber-loaded cavities are used. An estimate can be made, however, if we limit ourselves to an approximate calculation in a cavity in which the only losses are due to wall resistivity. In this case, we note that the stored energy is proportional to the energy density within the cavity integrated over its volume. The power loss, on the other hand, is proportional to the frequency times the energy density integrated through the volume of the resistive layer roughly skin deep at the cavity

* Different terminologies are used for these two contributions to Q. What is called the radiative Q here is sometimes called the diffractive Q — referring in particular to the diffractive output coupling from low group velocity devices such as gyrotrons — or the external Q. Our parasitic Q is also called the resistive Q — apt when the only cavity losses are due to wall losses — or the external Q, which applies when cavity losses are due primarily to radiation of unwanted mode energy through strategically placed wall slits.

wall. In this argument, we cancel out the energy density in the numerator and denominator of Equation 4.91 to obtain

$$Q_p = \frac{\text{cavity volume}}{(\text{surface area}) \times \delta} \times (\text{geometrical factor}) \tag{4.97}$$

where the geometrical factor is typically of the order unity (see Problem 8).

One might think that maximizing Q is desirable. Certainly, storing energy within the cavity increases the internal feedback, thus lowering the threshold for oscillation and reducing the demand on a power supply to produce the required electron beam current to drive an oscillator. In the world of HPM, however, high currents are relatively easy to produce, so that the challenge is shifted to the tasks of generating and handling high power in the cavity. From each standpoint — generating and handling high power — it is actually desirable to lower Q at high power. In the generation process, we shall see that the driving electron beam power is most effectively utilized when it is several times the threshold value; hence, raising the output power requires raising the threshold level, which translates to lowering Q. In handling microwave power, remember that the output power is proportional to the stored energy divided by Q, so that high Q implies high values of stored energy and larger electric fields in the cavity. This factor raises the wall heating rates and can lead to breakdown.

In closing our discussion of the quality factor, we touch on the issue of *fill time* for cavities, which is the time required for the fields in a cavity to build up to a steady-state level. Reasoning from Equation 4.91, it is apparent that the fill time is proportional to Q. For certain HPM applications involving cavities, fill time is an important additional consideration. In the accelerating cavity of an RF linac, for example, the goal is to transfer energy *to* electrons rather than extract it. Therefore, a trade-off must be made between raising Q to maximize the accelerating field and lowering Q to limit the fill time and resultant requirement it places on RF pulse lengths. As a second example, certain RF pulse compression schemes depend on the dynamic control of a cavity's Q in order to rapidly discharge the HPM energy that was slowly accumulated at lower power. The discharge time is roughly equal to the fill time, and switching to a lower Q permits this rapid discharge.

4.6 Intense Relativistic Electron Beams

High power microwave sources tap the kinetic energy of electrons in an intense relativistic beam or rotating layer to produce the intense microwave fields. To get an idea of the parameter range in which HPM devices operate, remember that the microwave power P is generated at some power efficiency η_P from an electron current I accelerated by a voltage V:

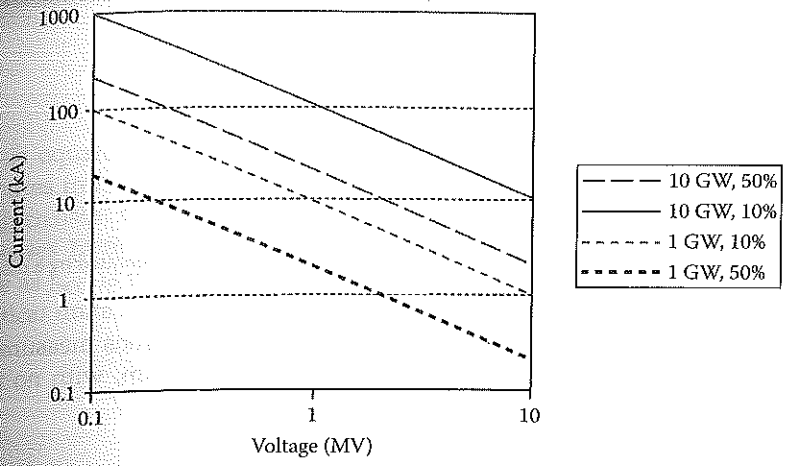

FIGURE 4.18
Beam voltage and current required to produce 1 and 10 GW of microwave output at power efficiencies η_P of 10 and 50%.

$$P = \eta_P VI \tag{4.98}$$

The microwave power in pulsed HPM sources is of the order of 1 to 10 GW, and efficiencies range from 10 to 50%. In Figure 4.18, we show the required current and voltage to reach 1 and 10 GW at efficiencies of 10 and 50%. One can see that currents of the order of 10 kA, or 10 s, are required for voltages around 1 MV. In most cases, this current is carried in a beam of a specified cross-sectional profile at a high current density (see Problem 9).

We defer the treatment of the technology of producing intense electron beams and layers to the next chapter, where we will discuss cathodes, diodes, and electron guns. In this chapter, though, we discuss the basics of electron flow in diodes — space-charge-limited electron flow in Child–Langmuir diodes (planar geometry) and Langmuir–Blodgett diodes (cylindrical geometry) — as well as the current limit imposed by the magnetic pinching of a high-current beam. Also, we consider electron flow along electron drift tubes and in magnetically insulated electron layers, all as background for our discussion of microwave interactions, which will follow.

4.6.1 Space-Charge-Limited Flow in Diodes

First, consider the one-dimensional planar geometry of Figure 4.19, with a cathode at x = 0 and an anode at x = d. The electric potential at the cathode is $\phi(x = 0) = 0$, and at the anode, $\phi(x = d) = V_0$. An electron current of density $\mathbf{j} = \hat{x}j(x) = -\hat{x}en(x)v_x(x)$ flows from the cathode to the anode, where –e is the

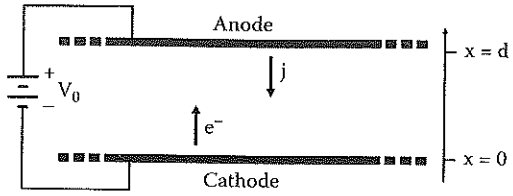

FIGURE 4.19
The ideal Child–Langmuir diode, with infinite parallel-plate electrodes separated by a distance d, with a voltage V_0 across the gap.

charge on an electron, n(x) is the number density of electrons measured in m^{-3}, and $v_x(x)$ is the velocity of an electron. In equilibrium, with no time dependence, ϕ and n are linked by Equation 4.4:

$$\frac{dE_x}{dx} = -\frac{d^2\phi}{dx^2} = -\frac{1}{\varepsilon_0} en \tag{4.99}$$

where we have replaced the electric field with the gradient of ϕ in this one-dimensional problem. For convenience, let us assume that $V_0 < 500$ kV, so that the problem is nonrelativistic; we therefore relate ϕ and v_x through the conservation of energy, assuming that the electrons leave the cathode with $v_x(0) = 0$:

$$\frac{1}{2} m v_x^2 = e\phi \tag{4.100}$$

with m the mass of an electron. We close this set of equations by taking the divergence of Ampere's law (Equation 4.1), remembering that $\partial E_x/\partial t = 0$, which yields

$$\frac{dj}{dx} = -e\frac{d(nv_x)}{dx} = 0 \tag{4.101}$$

This last equation tells us that nv_x is a constant across the gap, so for convenience, we define J, which is the magnitude of the current density across the gap,

$$J = env_x = \text{ constant} \tag{4.102}$$

although we note that we have reversed the sign of this constant from that of the current density. From this set of equations, we can find the following equation governing ϕ between the cathode and anode:

$$\frac{d^2\phi}{dx^2} = \left(\frac{m}{2e}\right)^{1/2} \frac{J}{\varepsilon_0 \phi^{1/2}} \tag{4.103}$$

In this equation, ϕ vanishes at the cathode. One can also show that as J increases from 0, so that the amount of space-charge in the anode–cathode gap increases, the magnitude of the electric field at the cathode, $d\phi/dx = \phi'$, decreases from V_0/d. The maximum current crossing the gap, which we write as J_{SCL}, is the value at which $\phi'(0) = 0$, which one can show is given in practical units by

$$J_{SCL}\left(\frac{kA}{cm^2}\right) = 2.33\frac{\left[V_0(MV)\right]^{3/2}}{\left[d(cm)\right]^2} \tag{4.104}$$

This is the *Child–Langmuir,*[11] or *space-charge-limited,* current density in a planar electron diode. Now if we can ignore edge effects, so that the current density is uniform across the surface of a cathode with area A, the current I from such a Child–Langmuir diode is $J_{SCL}A$ and the impedance Z for such a diode would be the ratio of the current to the voltage, or

$$Z = \frac{V_0}{I} = 429\frac{\left[d(cm)\right]^2}{A(cm^2)}\frac{1}{\left[V_0(MV)\right]^{1/2}}\ \Omega$$

As an example, a typical value for a diode is $V_0 = 1$ MV, with a gap of d = 1 cm and a cathode diameter of 2 cm. Therefore, $J_{SCL} = 2.33$ kA/cm², I = 7.32 kA, and Z = 137 Ω (see Problem 10).

Langmuir and Blodgett solved the same problem in the cylindrical geometry[12] of Figure 4.20. The cathode radius r_c can be either on the inside, so that $r_c = r_i$ and the anode radius $r_a = r_o$, or on the outside, so that $r_c = r_o$. Recasting the expression for $\nabla^2\phi$ in Equation 4.99 and the expression for $\nabla\bullet\mathbf{j}$ in the proper form for cylindrical geometry, and retaining Equation 4.100 in the same form, we find that the cylindrical analog of Equation 4.103 is

$$\frac{d^2\phi}{dr^2} + \frac{1}{r}\frac{d\phi}{dr} = \left(\frac{m}{2e}\right)^{1/2}\left(\frac{r_c}{r}\right)\frac{J}{\varepsilon_0\phi^{1/2}} \tag{4.105}$$

The space-charge-limited (meaning that the electric field at the cathode vanishes) solution to this equation yields an expression for the current density *at the cathode* that is similar in form to Equation 4.104:

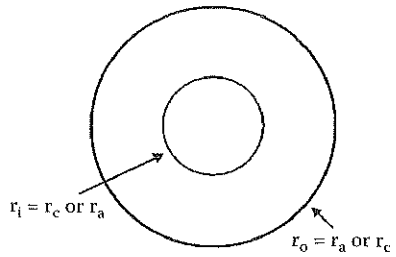

FIGURE 4.20
Cross-sectional view of the cylindrical Langmuir–Blodgett diode.

$$J\left(\frac{kA}{cm^2}\right) = 2.33\frac{\left[V_0(MV)\right]^{3/2}}{\left[r_a(cm)r_c(cm)\right]Y^2} \tag{4.106a}$$

with Y an infinite series solution with more than one form, depending on the ratio r_a/r_c and the desired accuracy of the solution.[12] The form of Y most appropriate for HPM diodes is

$$Y = \left(\frac{r_c}{r_a}\right)^{1/2}\sum_{n=1}^{\infty} B_n\left[\ell n\left(\frac{r_a}{r_c}\right)\right]^n \tag{4.106b}$$

where $B_1 = 1$, $B_2 = 0.1$, $B_3 = 0.01667$, $B_4 = 0.00242$, and so on (14 terms are given in the reference). Remember that Equation 4.106a gives the current density at the cathode of a cylindrical diode; to compute the current, one must multiply by the cathode area, $A_c = 2\pi r_c L$, where L is the length of the emitting area (see Problems 11 and 12).

Our treatments of the flow of electrons in either a planar or cylindrical diode are predicated on the assumption that the diode voltage is nonrelativistic — i.e., $V_0 < 500$ kV — so that the nonrelativistic form in Equation 4.100 applies. In the event that $V_0 > 500$ kV, a relativistic form for the planar Child–Langmuir diode was derived by Jory and Trivelpiece:[13]

$$J\left(\frac{\text{kA}}{\text{cm}^2}\right) = \frac{2.71}{\left[d(\text{cm})\right]^2}\left[\left(1+\frac{V_0(MV)}{0.511}\right)^{1/2} - 0.847\right]^2 \tag{4.107}$$

Note the identical scaling with the anode–cathode gap width in both Equations 4.103 and 4.107. The voltage scaling is quite different, however, with the familiar $V_0^{3/2}$ scaling at low voltages, while at high voltages $J \propto V_0$.

4.6.2 Beam Pinching in High-Current Diodes

In our treatment of the Child–Langmuir diode, we also assumed that the self-magnetic field of the beam current can be neglected. However, at high currents, the strong azimuthal self-magnetic field of the beam causes electron beams to pinch due to the Lorentz force $F_r = v_z \times B_\theta$. The critical beam current above which *beam pinching* occurs is estimated by equating the Larmor radius for an electron at the edge of the beam with the anode–cathode gap spacing:[14]

$$I_{\text{pinch}}(\text{kA}) = 8.5\frac{r_c}{d}\left[1+\left(\frac{V_0(\text{MV})}{0.511}\right)\right] \tag{4.108}$$

where r_c is the cathode electrode radius. Generally speaking, pinching would be a disaster in an HPM source and is to be avoided. This effect is a factor particularly in low-impedance diodes such as those used in virtual cathode oscillators (see Problem 13).

4.6.3 Space-Charge-Limited Electron Beam Flow in a Drift Tube

Once the electron beam has been generated, it will pass through a drift tube on its way to the microwave interaction region. For convenience, let us assume that the drift region is long enough that we can assume it is effectively infinitely long. In addition, we assume that the duration of the beam is long enough that an equilibrium is set up in which we can ignore time-dependent effects. In this case, the space-charge of the beam creates a purely radial electric field between the beam and the drift tube wall, and we can perform a line integral of that field to find the electric potential difference between the beam and the wall. This potential difference reduces the effective accelerating potential of the beam, an effect referred to as *space-charge depression* of the beam energy. Let us calculate the space-charge depression of the beam energy for a thin, annular beam, as shown in Figure 4.21.

For simplicity, we assume that the axial magnetic field is infinitely large and that the beam is infinitely thin (mathematically, the current density could be represented by a delta function in radius), with radius r_b, equal to the mean radius of the thin beam shown in the figure. There is no space-charge inside the drift tube except at $r = r_b$, so inside and outside the beam, the potential is given by

$$\frac{1}{r}\frac{d}{dr}\left(r\frac{d\phi}{dr}\right) = 0 \tag{4.109}$$

The boundary conditions are $d\phi/dx = 0$ at $r = 0$ and $\phi = 0$ at the wall, $r = r_0$. Thus,

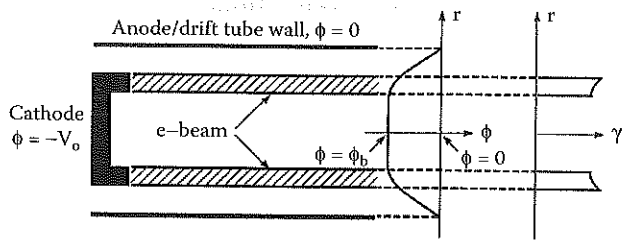

FIGURE 4.21
The potential, ϕ, and relativistic factor, γ, as a function of radius for electrons in an intense annular electron beam. Space-charge in the beam depresses the potential to $-\phi_b$ on the axis. The electron energy varies with radius across the beam (i.e., it is *sheared*), with the highest energy electrons at the outer edge of the beam.

$$\phi(r) = -\phi_b \ , \ 0 \le r < r_b \tag{4.110}$$

and

$$\phi(r) = A + B\ell n(r) \ , \ r_b < r \le r_0 \tag{4.111}$$

It remains to find ϕ_b in terms of r_b, r_0, and the space-charge in the beam, which depends on the beam current I_b and the beam velocity

$$v_b = c(1 - 1/\gamma_b^2)^{1/2}$$

In the expression for v_b, γ_b is the effective relativistic factor for the beam electrons; it is given by

$$\gamma_b = 1 + \frac{e}{mc^2}(V_0 - \phi_b) \equiv \gamma_0 - \frac{e\phi_b}{mc^2} \tag{4.112}$$

where $-V_0$ is the potential of the cathode from which the beam electrons were launched and γ_0 is as defined.

Let us eliminate A and B in Equation 4.111. First, ϕ must be continuous across the beam, so that we set $\phi(r_b) = -\phi_b$ in Equation 4.111. Next, we determine the discontinuity in $d\phi/dr$ at r_b by integrating Equation 4.109 across the beam:

$$r_b\left[\frac{d\phi(r = r_b^+)}{dr} - \frac{d\phi(r = r_b^-)}{dr}\right] = \frac{e}{\varepsilon_0}\int_{r_b^-}^{r_b^+} n_b r dr = \frac{1}{2\pi\varepsilon_0 v_b}\int_{r_b^-}^{r_b^+} e n_b v_b 2\pi r dr \tag{4.113}$$

$$= \frac{I_b}{2\pi\varepsilon_0 v_b}$$

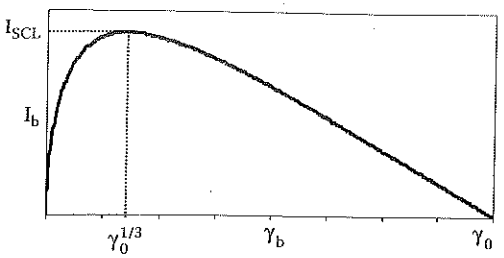

FIGURE 4.22
Plot of the beam current vs. the beam relativistic factor.

In this expression, I_b is the magnitude of the electron beam current. Note that the second term in the brackets on the far left side of this equation vanishes, while the first term is found by differentiating Equation 4.111. Using the continuity of ϕ at r_b, the vanishing of ϕ at r_0, and Equation 4.113, we find

$$I_b = \frac{2\pi\varepsilon_0 v_b}{\ell n(r_0/r_b)}\phi_b = \frac{8.5}{\ell n(r_0/r_b)}\left(1 - \frac{1}{\gamma_b^2}\right)^{1/2}(\gamma_0 - \gamma_b) \ \text{kA} \tag{4.114}$$

In this last expression, we have used Equation 4.112 to eliminate the space-charge potential term ϕ_b and the expression for v_b in terms of γ_b to find a relationship between I_b and the actual relativistic factor for the beam electrons, γ_b, which is less than γ_0 — what it would be if there were no space-charge depression.

Figure 4.22 is a plot of I_b vs. γ_b. We see that for each value of I_b, there could be two values of γ_b; in fact, the values of γ_b to the right of the current maximum are the correct values. Differentiating I_b in Equation 4.114 with respect to γ_b, we find that I_b is a maximum for $\gamma_b = \gamma_0^{1/3}$, at which value,

$$I_b(\gamma_b = \gamma_0^{1/3}) \equiv I_{SCL}(\text{annular}) = \frac{8.5}{\ell n(r_0/r_b)}(\gamma_0^{2/3} - 1)^{3/2} \tag{4.115}$$

We call I_{SCL} the *space-charge-limiting current* for the drift tube. Note here that I_{SCL} scales as $V_0^{3/2}$ at low voltages and as V_0 at large voltages, which is a scaling similar to that in the Child–Langmuir diode. In fact, this is the value for a thin, annular beam. One can show that for a beam with a uniform density over a solid cross section of radius r_b,

$$I_b(\gamma_b = \gamma_0^{1/3}) \equiv I_{SCL}(\text{solid}) = \frac{8.5}{1 + \ell n(r_0/r_b)}(\gamma_0^{2/3} - 1)^{3/2} \tag{4.116}$$

(see Problem 14).

One way to neutralize the space-charge fields of the beam, and thereby obviate the space-charge depression and limiting current, is to prefill the drift tube with plasma. As the electron beam passes through the plasma, its space-charge fields will rapidly expel enough plasma electrons that the beam space-charge will be compensated by the remaining plasma ions. An additional salutary effect is that the beam quality is improved by the reduction or elimination of radial variations in the electron velocities. The price one pays, of course, is the added complexity of generating the plasma, and the fact that recombination and further ionization of the plasma by the beam make the self-electric field time dependent.

4.6.4 Beam Rotational Equilibria for Finite Axial Magnetic Fields

When the axial magnetic field is reduced from very large values, at which it can effectively be considered infinite, I_{SCL} is reduced as well. Finite axial magnetic fields also cause the beam to rotate in equilibrium, which serves to balance the forces on the beam so that the net force vanishes. For convenience, consider a nonrelativistic beam. Using a quite general treatment based on the fluid equations, one can show that the azimuthal rotational velocity of electrons in a beam traveling in a cylindrical drift tube is given by[15]

$$v_{eb}^{\pm}(r)=\frac{1}{2}\Omega_{eb}r\left\{1\pm\left[1-4\frac{e^2}{\varepsilon_0 m\Omega_{eb}^2 r^2}\int_0^r dr' r' n_{eb}(r')\right]^{1/2}\right\} \tag{4.117}$$

where $\Omega_{eb} = eB_z/m$ is the electron cyclotron frequency of the beam electrons in the applied axial magnetic field B_z, with $-e$ and m the charge and mass of an electron, respectively, and n_{eb} the number density of beam electrons. We see that there are two rotational velocities possible for the beam electrons. To see their physical significance, consider the case in which the right-hand term under the square root in Equation 4.117 is much smaller than unity, so that to lowest order in that small quantity

$$v_{eb}^{+} \approx \Omega_{eb}r \tag{4.118a}$$

$$v_{eb}^{-} \approx \frac{e^2}{\varepsilon_0 m\Omega_{eb} r}\int_0^r dr' r' n_{eb}(r')=-\frac{E_r}{B_z} \tag{4.118b}$$

In this latter expression, we have used Equation 4.4 to make the replacement

$$E_r=-\frac{e}{\varepsilon_0 r}\int_0^r dr' r' n_{eb}(r')$$

Thus, the two rotational equilibria are designated as follows:

- *Slow rotational mode*, in which the rotational velocity v_{eb}^{-} of the electron guiding centers has the character of an $\mathbf{E}\times\mathbf{B}$ rotation, although the electrons, on the small scale of a Larmor orbit within the beam, still undergo cyclotron rotation at Ω_{eb} about their guiding centers.
- *Fast rotational mode*, in which the electrons as a whole rotate about the beam axis at a frequency approximately equal to the cyclotron rotational velocity, $\Omega_{eb}r$. Such beams are also called *axis-encircling beams*.

The slow rotational mode is the more commonly seen, although a beam can be induced into the fast rotational mode by passing a slow-rotational-mode beam through a magnetic cusp. Axis-encircling beams created in this way are used in so-called large-orbit gyrotrons (see Problem 15).

4.7 Magnetically Insulated Electron Layers

Not all sources use electron beams. Notably, the magnetron and magnetically insulated line oscillator (MILO) employ a magnetically insulated layer of electrons bounded on one side by an electrode at cathode potential. In this geometry, a magnetic field is applied parallel to the cathode surface, and electrons emitted from the cathode are deflected by the $\mathbf{v}\times\mathbf{B}$ Lorentz force and prevented from reaching the anode. Accordingly, they remain trapped in a layer adjoining the cathode, drifting in the $\mathbf{E}\times\mathbf{B}$ direction, parallel to the cathode. The situation is depicted in Figure 4.23.

The *Hull criterion* for magnetic insulation of the layer — meaning that in equilibrium the electrons cannot cross the gap to reach the anode — is derived from very general arguments based on the conservation of energy and canonical momentum in the direction of net electron drift. Assume that all electrons are emitted from the cathode, that there are no system variations along their direction of drift, and that a time-independent equilibrium is established. In the so-called *smooth-bore magnetron* with an axial magnetic field B_z within a cylindrical geometry with cathode radius $r_c <$ r_a, the anode radius, the electrons drift azimuthally at v_θ with their energy conserved, so that